IOPscience iopscience.iop.org

Home Search Collections Journals About Contact us My IOPscience

Raman scattering investigation of CN in annealed CoN/CN soft-x-ray multilayers

This article has been downloaded from IOPscience. Please scroll down to see the full text article.

1998 J. Phys.: Condens. Matter 10 3433

(http://iopscience.iop.org/0953-8984/10/15/019)

View the table of contents for this issue, or go to the journal homepage for more

Download details:
IP Address: 171.66.16.209
The article was downloaded on 14/05/2010 at 12:57

Please note that terms and conditions apply.

J. Phys.: Condens. Matter **10** (1998) 3433–3448. Printed in the UK PII: S0953-8984(98)86941-5

Raman scattering investigation of CN in annealed CoN/CN soft-x-ray multilayers

H L Bai and E Y Jiang

Department of Applied Physics, Tianjin University, Tianjin 300072, People's Republic of China

Received 12 August 1997, in final form 22 December 1997

Abstract. The Raman features of CN layers in annealed CoN/CN soft-x-ray multilayers, deposited by dual-facing-target sputtering, are investigated. The Raman spectra resemble that of amorphous carbon. The features that are different from those of Co/C multilayers (Bai H L, Jiang E Y and Wang C D 1996 *J. Appl. Phys.* **80** 1428) include: (1) the integral intensity ratio $I(\mathrm{D})/I(\mathrm{G})$ of the D line to the G line increases with the annealing temperature, but the peak feature observed at 600 °C in the $I(\mathrm{D})/I(\mathrm{G})$ versus temperature curve of the Co/C multilayers no longer exists; (2) in the temperature range of the annealing, the D-line position changes from 1352.1 to 1367.7 cm^{-1}, and the G-line position from 1553.7 to 1594.0 cm^{-1}; the D- and G-line positions for as-deposited M4–CoN/CN multilayers are much higher than those of Co/C multilayers, and close to those for polycrystalline graphite; (3) the linewidths of the D and G lines decrease with the increasing annealing temperature, and they are much lower than those for Co/C multilayers. These results indicate that the primary bonding in the CN sublayers is sp^2. In other words, the formation of the sp^3 bonding in the CN sublayers can be suppressed effectively by doping with N atoms, and thus the period expansion resulting from the changes in the density of the CN layers can be decreased considerably. With the low-angle x-ray diffraction measurements, we do observe a great decrease in period expansion.

1. Introduction

Carbon nitride materials containing varying amounts of nitrogen can be used in many technological applications such as in coatings for magnetic disk drivers and infrared windows. *Ab initio* theoretical calculations by Liu and Cohen [1] indicated a crystalline material, termed β-C_3N_4, with a structure similar to that of β-Si_3N_4, with tetrahedral and trigonal bonding configurations for the carbon and nitrogen atoms respectively. The bulk modulus of this material was predicted to be ($\sim$4.83 Mbar), comparable to those of diamond ($\sim$4.43 Mbar) and cubic boron nitride (c-BN) ($\sim$3.69 Mbar), and the cohesive energy was found by calculation to be moderately large. While the synthesis of pure β-C_3N_4 remains to be achieved, the nitrogen content in the resulting films is less than that in the predicted β-C_3N_4 phase (57%). The deficiency of nitrogen was generally attributed to:

(1) the energetic particle bombardments involved in the deposition process [2, 3]; and

(2) the existence of stable carbon nitride compounds (such as C_2N) other than β-C_3N_4, having an N-atom fraction lower than 57% [4].

The preparation techniques that have been tried so far include low-energy mass-selected ion-beam deposition [2, 5], dual-ion-beam deposition [6], particle-beam-assisted laser processing [7], reactive sputtering [8, 9], and electron-cyclotron-resonance-assisted evaporation [10].

0953-8984/98/153433+16$19.50 © 1998 IOP Publishing Ltd

Besides the above-stated applications, another important application of CN films is their use as space materials (space layer–spacer) for the soft-x-ray multilayers [11, 12], which consist of alternating layers of materials with low and high electron densities, generally referred to as the spacer and the absorber, respectively. In our study, CN monolayers and CoN/CN soft-x-ray multilayers were prepared by reactive dual-facing-target sputtering. The aim of nitrogen incorporation is to improve the thermal stability of CoN/CN multilayer mirrors operated in high-temperature environments. As is known, soft-x-ray multilayers are often used as reflectors under high-brilliance synchrotron radiation beams. The beams can produce a significant heat load on the mirror, and cause an increase in the temperature of several hundred degrees. Since multilayers are inherently metastable composites with nanometre-scale periodicities, their microstructural stability and the stability of their reflectance under thermal processing or intense x-ray flux are therefore of considerable interest. A possible way to avoid the high-temperature-induced damage, such as interdiffusion, crystallization and compound formation, is to make compound multilayers instead of elemental multilayers, i.e. both the absorber and the spacer can be made of relatively inert and stable compounds so that the tendency towards interdiffusion, and interfacial and intralayer crystallization is minimized.

Raman spectroscopy is nondestructive and is sensitive to changes in translational symmetry. Thus, it is often used to characterize carbon and carbon nitride materials. The aim of this paper is to reveal the changes in the bond structures of carbon through incorporating nitrogen, and the mechanisms reducing the period expansion of CoN/CN soft-x-ray multilayers at high annealing temperatures by Raman spectroscopy.

In this study, the structural evolution of CN sublayers in the annealed CoN/CN soft-x-ray multilayers was investigated by Raman spectroscopy (RS). As complementary techniques, low- and high-angle x-ray diffraction (LAXD and HAXD, respectively), transmission electron microscopy (TEM), and x-ray photoelectron spectroscopy (XPS) were also used to characterize the samples.

2. Experimental details

2.1. Multilayer fabrication

The multilayer samples were made by a dual-facing-target sputtering (DFTS) system, which has been designed in order to deposit multilayers without breaking the vacuum. The typical base pressure of the chamber was below 1×10^{-6} Torr. The targets, 10 cm in diameter, were of 99.99% purity Co and 99.999% purity C. During the deposition, the Ar pressure was kept at 4.0×10^{-3} Torr. The total pressure of Ar and N_2 gases was kept at 4.0×10^{-3} Torr, and the partial pressure of N_2 was fixed at (2.0, 4.0, 6.0, 8.0, 10.0) $\times 10^{-4}$ Torr. The multilayer samples prepared at the different nitrogen partial pressures are denoted as M1–M5, respectively. The typical deposition rates were 0.03 nm s^{-1} for CoN, and 0.01 nm s^{-1} for CN. The sublayer thickness was monitored by a quartz crystal oscillator. Layering was accomplished by the sequential rotation of the substrate over pure Co and C sputter sources. A series of CoN/CN multilayers were fabricated on ultra-smooth crystalline (111) silicon wafers and NaCl crystals with a freshly cleaved surface. No attempt was made to remove the natural oxide layer on the silicon wafers prior to the deposition. Each multilayer begins with a CN layer and ends also with a CN layer, and the last CN layer is made twice as thick as the other sublayers in order to retard the oxidation. The nominal structures are periods of 5.0 nm with a ratio of the thickness of the CoN layer to the multilayer period of $\Gamma = 0.4$. The temperature inside the chamber during the deposition was below 100 °C. No

attempt was made to control the substrate temperature throughout the deposition.

X-ray photoelectron spectroscopy (XPS), a surface-sensitive probe, cannot give the real concentration profiles of the multilayers because (1) the atomic concentration profiles of multilayers with a layer spacing approaching the escape depth of the photoelectrons may suffer from severe spatial resolution limitations, and (2) the sputter-induced roughness, interfacial broadening, atomic mixing, and preferential etching can also degrade the spatial resolution of the profile. In order to obtain the real atomic fractions of N in the CoN and CN sublayers, we also prepared CoN and CN monolayers under the same conditions as those for which the sublayers were fabricated. The thickness of the monolayers is about 100 nm.

2.2. Annealing treatment

Two types of annealing were performed, the classical thermal annealing in a vacuum furnace and the *in situ* annealing in a transmission electron microscope (TEM). Classical annealing was performed in a furnace at 10^{-6} Torr pressure for 30 min at different annealing temperatures. The temperature was measured with a NiCr–NiAl thermocouple and controlled within ± 1 °C. The samples for transmission electron microscopy (TEM) were heated *in situ* in the microscope, and the same annealing procedure followed as in the classical anneal.

2.3. Sample characterization

2.3.1. Low- and high-angle x-ray diffraction (LAXD and HAXD, respectively). All of the x-ray diffraction investigations used Cu Kα lines with a wavelength $\lambda = 0.154$ nm. The multilayer period Λ was calculated from the Bragg equation, modified for refraction [13, 14]:

$$\sin^2(\theta_m) = \left(\frac{m\lambda}{2\Lambda}\right)^2 + 2\delta \tag{1}$$

where Λ is the modulation period, m the integer reflection order number, and δ the average deviation of the refractive index from unity. Using equation (1), Λ and δ can be determined from the linear regression of the $\sin^2\theta_m$ versus m^2 plot.

Standard θ–2θ high-angle x-ray diffraction was used here to identify the phases presented in the as-deposited and annealed CoN/CN multilayers.

2.3.2. Transmission electron microscopy (TEM). The samples deposited on the NaCl (100) single crystal were examined using a JEM-200CX transmission electron microscope operated at 200 kV. Selected-area electron diffraction (SAED) and bright-field imaging were employed to characterize the structures of the as-deposited and annealed CoN/CN multilayers.

2.3.3. Raman spectroscopy (RS). Raman spectroscopy is a powerful tool for the characterization of carbon. The room temperature Raman measurements were performed by back-scattering from the sample with an argon-ion laser operating at 514.5 nm at a power of 150 mW. First-order Stokes spectra were detected with a Spex 1403 double monochromator, usually scanning between 1000 cm^{-1} and 1800 cm^{-1}. The structures of the CN in the multilayers before and after annealing were characterized by the Raman spectra.

2.3.4. X-ray photoelectron spectroscopy (XPS). XPS spectra were recorded in a Perkin–Elmer PhI 5300 spectrometer equipped with a spherical capacitor analyser, using Mg Kα radiation (1253.6 eV). The background pressure in the analysis chamber was maintained at 2.2×10^{-10} Torr. The operating pressure was less than 1.5×10^{-9} Torr.

In order to remove the contaminated surface layer, Ar ions with 2 keV energy and a current density of 1 μA mm^{-2} were used to sputter the samples.

3. Spectral decomposition

As will be discussed in subsections 5.2 and 5.3, the Raman spectra of the CoN monolayers and CoN/CN multilayers resemble those of amorphous carbon. The spectra can thus be analysed quantitatively using a computer to reproduce the data as a sum of bands with Gaussian or Lorentzian line shapes. The fitting parameters are the line position, relative integrated intensity and full width at half-maximum (FWHM), where the line position and FWHM are given for a fitting error below 10 cm^{-1}.

The Lorentzian line shape is based on the model proposed by DiDomenico *et al* [15] assuming a linear background. This model states that the intensity of the Raman spectrum is related to the frequency by

$$\frac{\mathrm{d}I}{\mathrm{d}\omega} \propto \frac{N\Gamma\omega_0^3}{(\omega_0^2-\omega^2)^2+4\Gamma^2\omega_0^2\omega^2} + b\omega + c \tag{2}$$

where $\mathrm{d}I/\mathrm{d}\omega$ is proportional to the detector signal at ω, ω_0 is the undamped mode frequency, and ω the frequency shift from the laser line. Γ is a damping factor and N a fitting constant. The fitted parameters were used to reproduce the Raman spectrum. The intensity of the two lines can be integrated, and the intensity ratio of the two lines is given by $N_\mathrm{D}/N_\mathrm{G}$, in which the subscripts D and G stand for the D and G lines, respectively. The linewidth $\Delta\omega$ is equal to $2\Gamma\omega_0$.

The Gaussian line shape can be expressed as

$$I \propto A\exp\left(\frac{-(\omega-\omega_0)^2}{2\Delta^2}\right) \tag{3}$$

where A is the amplitude and Δ the linewidth, i.e. the full width at half-maximum (FWHM). The Raman intensity of the Gaussian line shape is integrated, and the intensity ratio of the two lines is easily obtained.

4. General description for the Raman spectra of carbon

4.1. Vibrations

Hexagonal graphite has a crystal structure built up of flat layers in which the trivalent carbon atoms occupy the lattice sites of a two-dimensional honeycomb network, as shown in figure 1. The layers are stacked in a hexagonal crystal structure corresponding to the space group $P6_3/mmc$ ($\mathrm{D}_{6\mathrm{h}}^4$). The primitive cell contains four atoms, two atoms shown in one layer and another two atoms in an adjacent layer. In single-crystal graphite, the shortest interatomic distance is 1.42 Å in the planes, while the distance between the consecutive planes is 3.354 Å. In other types of graphite, the covalent bond distance of 1.42 Å is always preserved, but the interlayer distance can have values ranging from 3.354 to 3.7 Å.

The number of frequencies expected in the Raman spectrum of single crystals of graphite can easily be evaluated. There are four atoms in the primitive cell, so the phonon dispersion

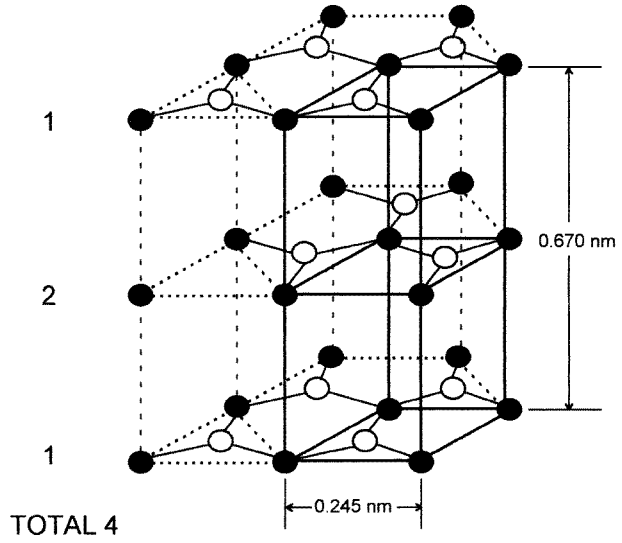

Figure 1. The crystal structure of graphite; the numbers on the left-hand side indicate the numbers of atoms in each layer of the primitive cell.

relation will reveal nine ($3n - 3 = 3 \times 4 - 3 = 9$) optical branches. Raman activity for a crystal can only be observed in the limit where the wave vector $\boldsymbol{K} \sim \mathbf{0}$, because for the visible exciting radiation the light scattering wave vector is $\sim 1/1000$ of the Brillouin zone dimension. A group theoretical analysis [16] of the graphite structure which has space group D^4_{6h} indicates that the zone-centre optical modes can be decomposed into the following irreducible representations:

$$\Gamma_{opt} = 2E_{2g} + E_{1u} + A_{2u} + 2B_{2g}. \tag{4}$$

The mode species and atomic displacements are shown in figures 2(a)–2(d). The E-symmetry modes exhibit 'in-plane' atomic displacements while the A- and B-symmetry modes have 'out-of-plane' displacement. Only the $2E_{2g}$ modes are expected to be Raman active, and they can be observed at $\sim$42 and $\sim$1580 cm^{-1} [17]. The A_{2u} and E_{2u} modes are IR active, and they can be observed at $\sim$867 and $\sim$1588 cm^{-1}, respectively [18]. The B_{2g} modes are optically inactive; however, one has been observed via neutron scattering at 127 cm^{-1} [19, 20]. The two different E_{2g} modes in this *three-dimensional* analysis occur because adjacent planes can vibrate in phase or with opposite phase. The difference in energy between the two E_{2g} modes will be very small due to the relatively weak interlayer forces. In single crystals of graphite, the two E_{2g} modes will probably not show a measurable frequency separation and will appear as one single band.

For graphitic materials other than single crystals, it is reasonable to analyse the vibrating modes using only one layer of atoms. For a primitive cell containing only two atoms, the analysis gives for the resulting modes

$$\Gamma_{opt} = E_{2g} + B_{2g}. \tag{5}$$

Only the E_{2g} mode is Raman active, so only one band is expected in the two-dimensional analysis.

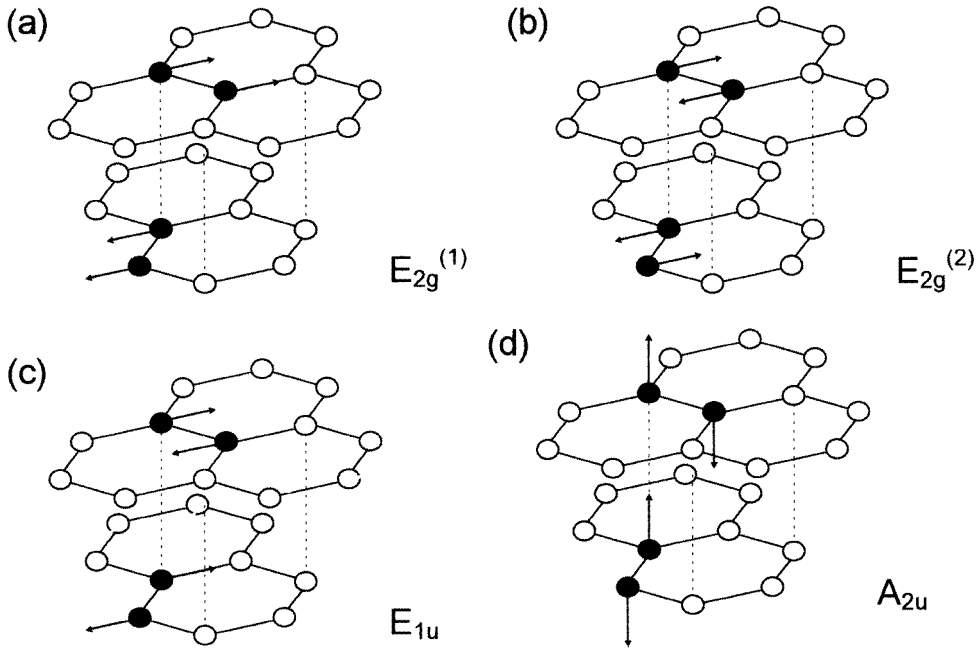

Figure 2. The optically active modes of graphite single crystal. (a) $E_{2g}^{(1)}$, (b) $E_{2g}^{(2)}$, (c) E_{1u}, (d) A_{2u}.

4.2. Bond structures of amorphous carbon

Generally, amorphous carbon (a-C) is considered as a mixture of sp^3 (diamond-like) and sp^2 (graphite) bonding structure [21, 22], but its detailed bond structure is controversial. Kakinoki *et al* [23] suggested a two-phase model in which regions containing only threefold-coordinated atoms are bonded to regions containing only fourfold-coordinated atoms. Although this model could account for the lower density of a-C very well, it cannot explain the peak downshift observed in the as-deposited a-C films [24, 25]. As is known, the Raman scattering cross section of diamond (9.1×10^{-7} cm^{-1} sr^{-1}) is nearly two orders of magnitude lower than that of graphite (5×10^{-5} cm^{-1} sr^{-1}) [24]. For the inhomogeneous structure having large diamond-like regions connected by large graphitic regions, the contribution from tetrahedral bonds might not be noticeable. The Raman band of the a-C films thus originates only from the carbon cluster with the sp^2 configuration whose Raman spectrum contains a D line and a G line at about 1355 cm^{-1} and 1600 cm^{-1} [26], respectively. Therefore, the low-frequency shift found in as-deposited amorphous carbon is hard to understand within Kakinoki's inhomogeneous model.

Beeman *et al* [22] has developed a model starting from the assumption that certain percentages of fourfold-coordinated atoms are distributed uniformly throughout the threefold-coordinated atoms with bond-angle disorder, and that the bond angle is changed from the ideal 120° to a disordered average of $117.7^\circ \pm 5^\circ$. In the calculated spectra, both peaks are shifted down in frequency, with the G-line shift approximately proportional to the percentage of fourfold-coordinated atoms. When the model contains 51% fourfold-coordinated atoms, no major features appear at 1332 cm^{-1}, where a Raman peak is found for diamond. Thus, the effect of uniformly distributed tetrahedrally bonded atoms is to modify the vibration spectrum of the model as a whole, rather than to introduce spectral

features of scattering from 'diamond atoms'. Yoshikawa *et al* [21] also suggested that the tetrahedrally bonded carbon atoms might have an *indirect* influence on the Raman spectrum profile of a-C films through the interaction with trigonally bonded carbon atoms.

4.3. Raman spectra of small graphite crystallites

The most important differences in Raman spectra between graphite and small graphite crystallites are the appearance of the 'D' line at 1355 cm^{-1} which is assigned to the phonon associated with finite crystallite size, and the upward shift of the G line. These striking features can be interpreted as follows. Raman spectra are associated with the inelastic scattering process, and follow the law of conservation of energy and the rule of wave-vector selection:

$$\begin{aligned} \omega_s &= \omega_i \pm \omega \\ \boldsymbol{K}_s &= \boldsymbol{K}_i \pm \boldsymbol{K} \end{aligned} \tag{6}$$

where '+' and '−' correspond to anti-Stokes and Stokes scattering, respectively. The subscripts i and s denote incident and scattering radiation, respectively. ω and $\boldsymbol{K}$ are the frequency and wave vector of the phonons, respectively, involved in the scattering process. Therefore, Raman spectra are very sensitive to changes that disrupt the translational symmetry of the materials studied, such as occur in amorphous materials or small-dimension crystals.

As long-range translational symmetry is lost, equations (6) need no longer hold, and phonons with any vector $\boldsymbol{K}$ throughout the Brillouin zone may contribute to the Raman spectrum. Thus, the Raman spectrum of disordered materials may include information concerning phonons whose $\boldsymbol{K}$-vectors near the edge of the Brillouin zone, while the Raman spectrum of perfect crystal only concerns the case where $\boldsymbol{K} \sim \boldsymbol{0}$.

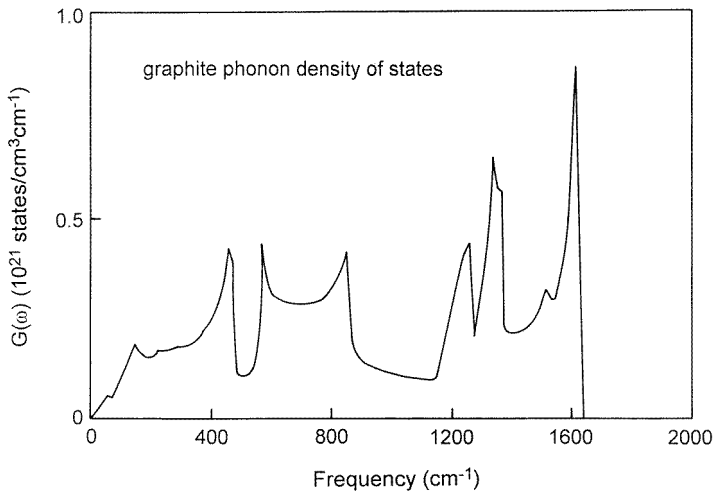

Figure 3. The phonon density of states (DOS) of graphite [27].

The spectra of disordered materials or small-dimension crystals favour phonons associated with large electron–phonon coupling constants as well as those associated with large densities of phonon states. The phonon dispersion curves of amorphous materials are similar to those of crystalline materials. Meanwhile, in the first-order approximation, the distribution

of the phonon density of states (DOS) of the amorphous material is also similar to that of the crystalline material except the increased width. The phonon density of states (DOS) [27] of graphite is shown in figure 3. The appearance of the D line and the upward shift of the G line are then explained by the large density-of-states peaks at $\boldsymbol{K} \neq \mathbf{0}$ points in the Brillouin zone.

Table 1. The N-atom fractions of the different CoN/CN multilayers.

No	N (at.%) (CoN layer)	N (at.%) (CN layer)
M1	9.1	13.0
M2	12.3	14.5
M3	13.0	18.0
M4	17.4	20.6
M5	15.3	18.7

5. Results and discussion

5.1. Structure characterization for as-deposited multilayers

The N-atom fractions in the CoN and CN monolayers can be used to represent the real chemical composition of the CoN and CN sublayers, because they were deposited under the same conditions. After 5 min of Ar^+-ion bombardment, the C peaks related to contamination and the oxygen peaks disappeared. The N-atom fractions of the different CoN/CN multilayers calculated using the integrated peak intensity and relative sensitivity factors are listed in table 1. The M4 sample possesses the highest N concentration.

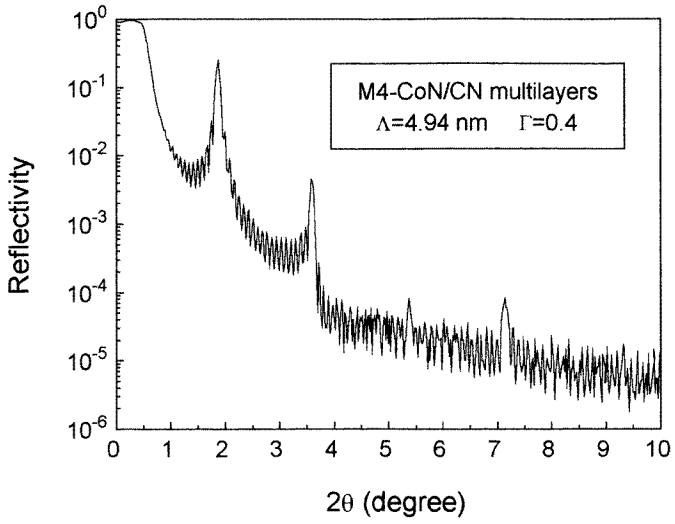

Figure 4. The low-angle x-ray diffraction (LAXD) pattern of M4–CoN/CN multilayers with a nominal period of 5.0 nm.

Figure 4 shows the LAXD peaks induced from the compositionally modulated structure of the M4–CoN/CN multilayers, with a nominal modulation period of 5.0 nm. The four

Table 2. The characters of different CoN/CN multilayers. 'Nom' designates the data obtained from the nominal structure. 'fit' denotes the data obtained from fitting results.

	Λ		δ (10^{-5})
No	Nom	Fit	Fit
M1	5.00	4.92	1.223
M2	5.00	5.02	1.197
M3	5.00	4.96	1.185
M4	5.00	4.94	1.145
M5	5.00	5.04	1.165

measured Bragg peaks indicate a relatively well compositionally modulated structure. The modulation period Λ and δ derived from the positions of the modulation peaks are listed in table 2.

Figures 5(a) and 6(a) show the HAXD spectrum, and the SAED pattern and electron micrograph of as-deposited M4–CoN/CN multilayers with a nominal period of 5.0 nm,

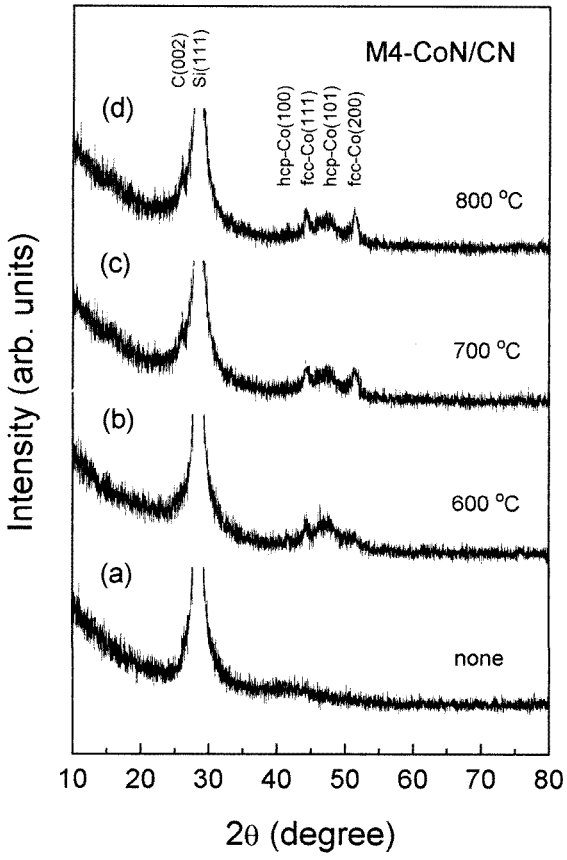

Figure 5. The high-angle x-ray diffraction (HAXD) patterns of M4–CoN/CN multilayers annealed at different temperatures.

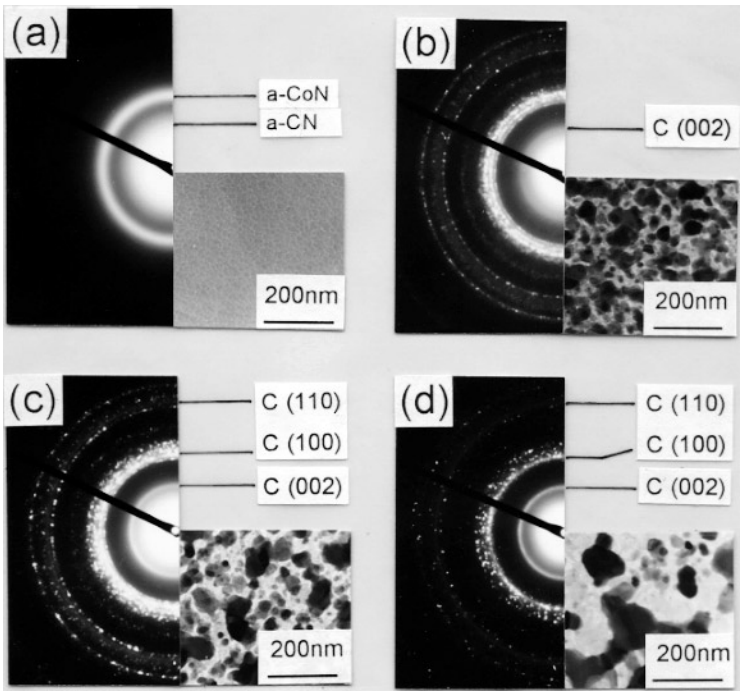

Figure 6. Selected-area electron diffraction (SAED) patterns and electron micrographs of M4–CoN/CN multilayers annealed at different temperatures. (a) As-deposited, (b) annealed at 600 °C, (c) annealed at 700 °C, (d) annealed at 800 °C.

indicating that the as-deposited M4–CoN/CN multilayers are amorphous. Although not presented here, the HAXD and TEM analyses of other as-deposited CoN/CN multilayers also give evidence of amorphism.

Table 3. Fitted Raman parameters of CN films.

			D line		G line	
Film	Type of fitting	$I(D)/I(G)$	Position	Width	Position	Width
CN	Lorentzian	2.42	1358.1	372.3	1547.0	173.4
	Gaussian	2.35	1364.9	368.5	1553.2	166.2

5.2. The Raman spectrum of the CN monolayers

Presented in figure 7 is the Raman spectrum of the CN monolayers, which resembles those of diamond-like carbon. The spectrum was decomposed with Lorentzian (figure 7(a)) and Gaussian (figure 7(b)) line shapes. The fitting results are shown in table 3. It is obvious that the two kinds of decomposition give nearly identical results within experimental error. We thus only use Gaussian lines to fit the spectra of the CoN/CN multilayers annealed at different temperatures.

Figure 7(c) shows the Raman scattering of the CoN monolayers. The spectrum cannot present any vibration information for frequencies ranging from 1000 to 1800 cm^{-1}.

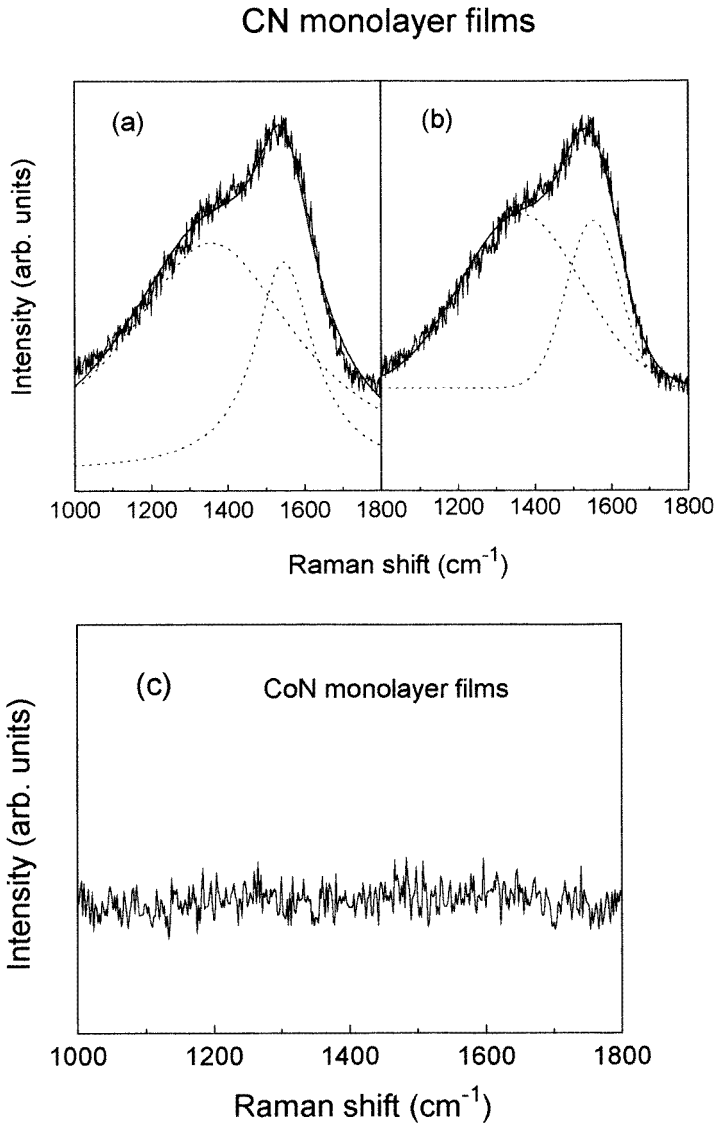

Figure 7. The Raman spectra of CN ((a), (b)) and CoN (c) monolayers.

Therefore, the Raman spectra of CoN/CN multilayers, scanned from 1000 to 1800 cm^{-1}, result only from the CN sublayers.

5.3. Thermal evolution of the Raman spectra of CoN/CN multilayers

In this subsection, the changes of the Raman spectra of annealed CoN/CN multilayers will be presented in detail. The influence of nitrogen incorporation on the bond formation is also discussed.

Figure 8 shows the temperature dependence of the Raman spectra of M4–CoN/CN multilayers. The Gaussian fitting results are shown in figure 9. Also shown in the figure

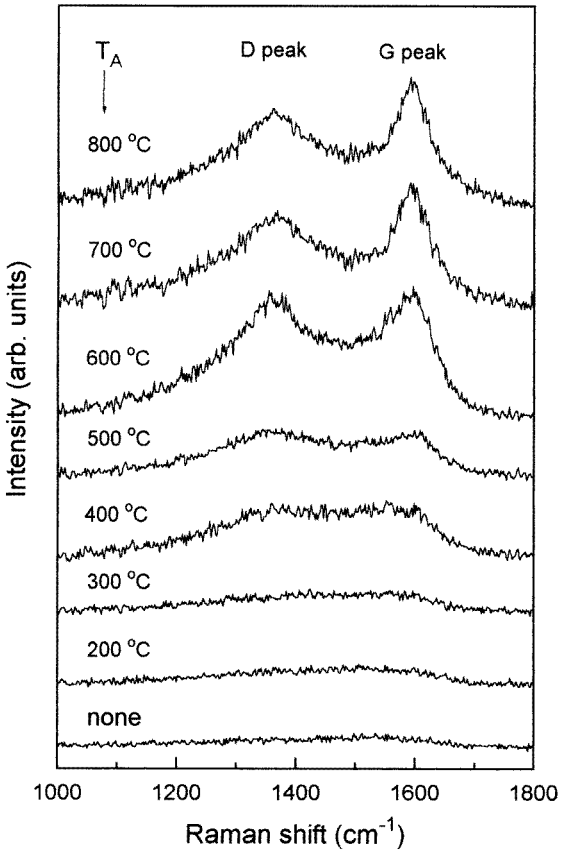

Figure 8. The temperature dependences of the Raman spectra of M4–CoN/CN multilayers.

are the fitting results of Co/C multilayers. Next, the temperature dependence of the fitting parameters, relative integrated intensity, line position, and full width at half-maximum (FWHM) will be discussed separately.

5.3.1. The relative integrated intensity ratio $I(D)/I(G)$. As shown in figure 9 (top left-hand panel), the integral intensity ratio of the D line to the G line increases with annealing temperature, but the peak feature observed at 600 °C in the $I(\mathrm{D})/I(\mathrm{G})$ versus temperature curve for Co/C multilayers no longer exists [28]. The intensity ratio $I(\mathrm{D})/I(\mathrm{G})$ is roughly proportional to the ratio of momentum-nonconserving phonons to conserving phonons which contribute to the Raman spectra. At low annealing temperatures (below 400 °C), very small crystallites are likely to exist in the carbon layers, but they are only weakly coupled to the incoming laser beam due to their small size and number, and thus contribute little to the Raman spectra. As the annealing temperature is increased (above 500 °C), the crystallites grow in number or size as confirmed by HAXD (figures 5(b)–5(d)) and TEM (figures 6(b)–6(d)). Thus, they begin to contribute to the Raman spectrum, causing the $I(\mathrm{D})/I(\mathrm{G})$ ratio to increase.

Vidano and Fischbach [29] stated that at higher annealing temperatures graphitization has occurred if the intensity ratio goes to zero. At higher annealing temperatures, graphitic crystallites grow larger, the effect of momentum conservation begins to increase in importance, and thus the $I(\mathrm{D})/I(\mathrm{G})$ ratio starts to decrease. Thus the decrease of the

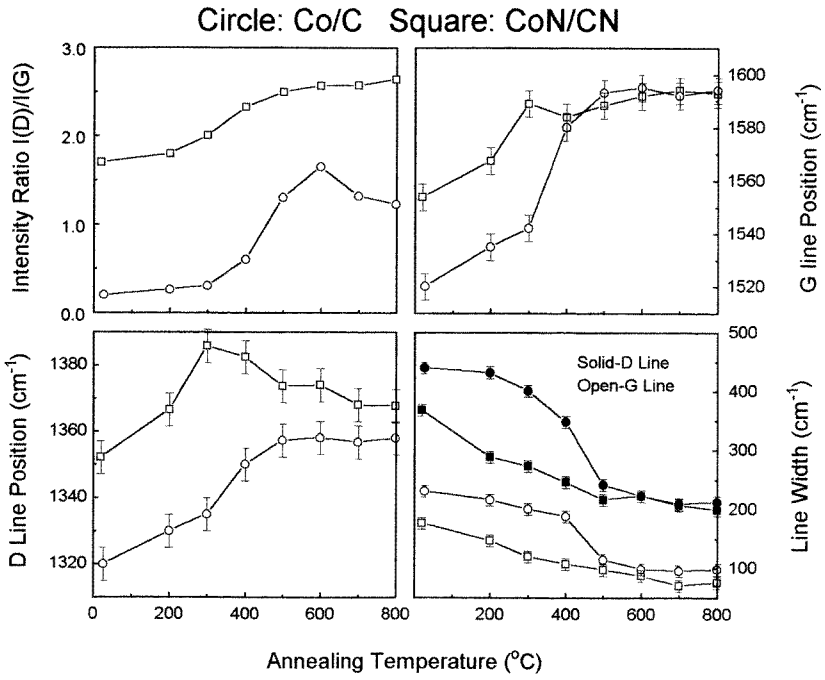

Figure 9. The Gaussian decomposition of the Raman spectra of annealed CoN/CN multilayers.

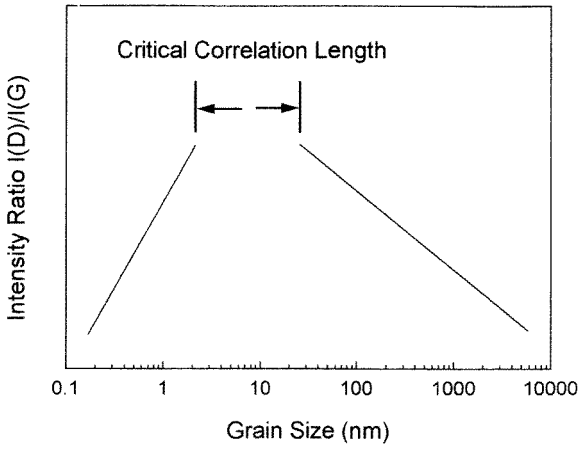

Figure 10. The relation between the relative intensity $I(\mathrm{D})/I(\mathrm{G})$ and the grain size.

$I(\mathrm{D})/I(\mathrm{G})$ ratio in Co/C multilayers can be interpreted as an increase in the dimensions of crystallites above some annealing temperature. The disappearance of the peak feature in the $I(\mathrm{D})/I(\mathrm{G})$ versus temperature curve of annealed CoN/CN multilayers implies that the ordered range of sp^2 is not large enough to make the intensity ratio decrease at higher annealing temperatures.

It is clear that the intensity ratio $I(\mathrm{D})/I(\mathrm{G})$ can be used to get a quantitative estimation of the sp^2 cluster size (the sp^2 correlation length). A critical correlation length should exist, which makes $I(\mathrm{D})/I(\mathrm{G})$ a maximum. Below the critical correlation length, the Raman

measurement on graphite at a different degrees of disorder suggested the functional relation

$$I(\mathrm{D})/I(\mathrm{G}) \propto L \tag{7}$$

where L is the typical graphite cluster size. When the samples are annealed, the grain size increases, and the rule of wave-vector selection will be conserved. In this case, the relation between relative intensity and grain size can be expressed as

$$I(\mathrm{D})/I(\mathrm{G}) \propto L^{-1}. \tag{8}$$

In figure 10, we show the two relations phenomenologically. The critical correlation lengths are usually on the scale of tens of nanometres. In our case, for Co/C multilayers, the critical correlation length is ∼3.5 nm [28].

5.3.2. D- and G-line positions. According to the amorphous carbon model proposed by Beeman, the line positions contain information concerning bond-angle disorder and the bonding in the crystallites that form. The upward shift of the line upon annealing suggests that some bond-angle disorders have been annealed out, and that the small percentage of tetrahedral bonds have been broken and have transformed to trigonal bonds.

As shown in figure 9 (top right-hand and bottom left-hand panels), in the temperature range of the annealing, for M4–CoN/CN multilayers, the D-line position changes from 1352.1 to 1367.7 cm^{-1}, and the G-line position from 1553.7 to 1594.0 cm^{-1}. The D- and G-line positions are much higher than those of Co/C multilayers [28], and close to that of polycrystalline graphite.

5.3.3. D and G linewidths. With the increase of annealing temperature, the observed decrease in linewidth of the D and G lines indicates the removal of bond-angle disorder and the increasing dominance of crystallites. In the as-deposited films, the linewidth becomes very large because of the bond-angle disorder (figure 9 (bottom right-hand panel)), and it narrows when the disorder is removed, and crystallites become more dominant upon annealing.

The linewidths of the D and G lines decrease with the increasing annealing temperature, and they are much lower than those of Co/C multilayers [28].

5.4. The effect of nitrogenation

These Raman features, especially the line positions, indicate that the primary bonding in the CN sublayers is sp^2. The disappearance of the peak feature in the $I(\mathrm{D})/I(\mathrm{G})$ versus temperature curve of CoN/CN multilayers (see figure 9) implies that the ordered range of sp^2 is not large enough to make the intensity ratio decrease at higher annealing temperatures. The lower linewidths give evidence of lower disorder in CN sublayers.

Since nitrogen does not form a solid at room temperature, it must be bonded with carbon in some way. In order to further clarify the C–N bonding, we measured the Raman spectrum of M4–CoN/CN multilayers, scanned from 1800 to 2600 cm^{-1}, as shown in figure 11. Also shown in the figure is the spectrum of CN monolayers. The peak at 2230 cm^{-1}, characteristic of carbon–nitrogen bond stretching, indicates that nitrogen is mainly chemically bonded to carbon with sp^2 bonding in the CN sublayers [30].

We would like to mention that it is not very clear how nitrogen affects the formation of sp^3 bonding, but we can tentatively explain the results as follows. The effects of N inclusion in sp^2 and sp^3 bonding should be very different. When an N atom, having a coordination number of three, substitutes for a sp^3-coordinated C atom, whose coordination number is

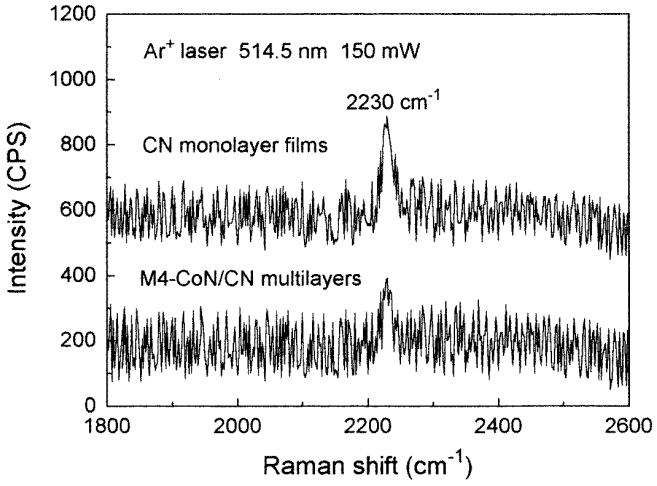

Figure 11. The Raman spectra of CoN monolayers and M4–CoN/CN multilayers, scanned from 1800 to 2600 cm^{-1}.

four, the average coordination number of the network is reduced. On the other hand, since the electronegativity of nitrogen is larger than that of carbon, the electron clouds between C–N bonds tend to locate near to the N atoms, and the C–C bonds will be weakened. As a consequence, the tetrahedral structures will collapse. If N atoms enter the sp^2 bonds, the coordination number will not change. Moreover, it is believed that the presence of nitrogen will change the nature of the density of states (DOS) of amorphous carbon, which is closely associated with the Raman spectroscopy, but how the N atoms affect the DOS also needs to be clarified.

The graphitization of CN layers will induce a density reduction, and thus a period expansion. Because the formation of sp^3 bonding can be effectively suppressed through doping with N atoms, and the transformation of sp^3 to sp^2 bonding on annealing will be attenuated significantly, and the period expansion of CoN/CN multilayers should be much smaller. With the small-angle x-ray diffraction measurements, as shown in figure 12, we did observe a smaller period expansion.

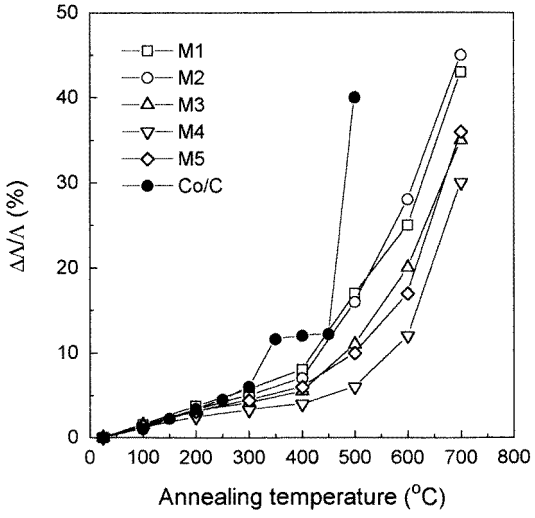

Figure 12. The expansion of the relative periods of annealed CoN/CN multilayers.

6. Conclusion

The Raman spectra of CN layers in annealed CoN/CN soft-x-ray multilayers, deposited by dual-facing-target sputtering, have been investigated. The results indicate that the primary bonding in the CN sublayers is sp^2. The formation of the sp^3 bonding in the CN sublayers can be suppressed effectively by doping with N atoms, and thus the period expansion resulting from the changes in the density of the CN layers can be decreased considerably. With the low-angle x-ray diffraction measurements, we do observe a great decrease in period. The results imply that nitrogen incorporation is an effective method for improving the thermal stability of Co/C soft x-ray multilayers. However, how nitrogen affects the formation of sp^3 bonding still needs to be clarified.

Acknowledgments

This work was financially supported by the Doctoral Programme Foundation of the State Education Commission, Tianjin Youth Science Foundation of the 21st Century and Youth Foundation of Tianjin University for Science Subjects.

References

[1] Liu A Y and Cohen M L 1989 *Science* **245** 841
[2] Marton D, Al-Bayati H A, Todorov S S, Boyd K J and Rabalais J W 1994 *Nucl. Instrum. Methods* B **90** 277
[3] Sjöström H, Ivanov I, Johanson M, Hultman L, Sundgren J-E, Hainsworth S V, Page T F and Wallenberg L R 1994 *Thin Solid Films* **246** 103
[4] Fang P H 1995 *J. Mater. Sci. Lett.* **14** 536
[5] Marton D, Boyd K J, Al-Bayati H A, Todorov S S and Rabalais J W 1994 *Phys. Rev. Lett.* **73** 118
[6] Song H W, Cui F Z, He X. M, Li W Z and Li H D 1994 *J. Phys.: Condens. Matter* **6** 6125
[7] Niu C, Lu Y Z and Lieber C M 1993 *Science* **261** 334
[8] Kumar S and Tansley T L 1994 *J. Appl. Phys.* **76** 4390
[9] Kaufman J H, Metin S and Saperstein D D 1989 *Phys. Rev.* B **39** 13 053
[10] Bousetta A, Lu M, Bensaoula A and Schultz A 1994 *Appl. Phys. Lett.* **65** 696
[11] Bai H L, Jiang E Y, Wang C D and Tian R Y 1997 *J. Phys.: Condens. Matter* **9** L205
[12] Bai H L, Jiang E Y and Wang C D 1997 *Thin Solid Films* **304** 278
[13] Agarwal B K 1979 *X-ray Spectroscopy* vol 15 (Berlin: Springer) p 134
[14] Henke B L, Uejio J Y, Yamada H T and Tackaberry R T 1986 *Opt. Eng.* **25** 937
[15] DiDomenico M Jr, Wemple S H, Porto S P S and Bauman R P 1968 *Phys. Rev.* **174** 522
[16] Mani K K and Ramani R 1974 *Phys. Status Solidi* b **61** 659
[17] Nemanich R J, Lucovsky G and Solin S A 1975 *Proc. Int. Conf. on Lattice Dynamics* ed M Balkanski (Paris: Flammarion) p 619
[18] Nemanich R J, Lucovsky G and Solin S A 1977 *Solid State Commun.* **23** 117
[19] Dolling G and Brockhouse B N 1962 *Phys. Rev.* **128** 1120
[20] Nicklow R, Wakabayashi N and Smith H G 1972 *Phys. Rev.* B **5** 4951
[21] Yoshikawa M, Katagiri G, Ishida H, Ishitani A and Akamatsu T 1988 *Solid State Commun.* **66** 1177
[22] Beeman D, Silverman J, Lynds R and Anderson M R 1984 *Phys. Rev.* B **30** 870
[23] Kakinoki J, Katada K, Hanawa T and Ino T 1960 *Acta Crystallogr.* **13** 171
[24] Wada N, Gaczi P J and Solin S A 1980 *J. Non-Cryst. Solids* **35+36** 543
[25] Elman B S, Dresselhaus M S, Mazurek H and Shaygan M 1982 *Phys. Rev.* B **25** 4142
[26] Dillon R O, Woollam J A and Katkanant V 1984 *Phys. Rev.* B **29** 3482
[27] Al-Jishi R and Dresselhaus G 1982 *Phys. Rev.* B **26** 4514
[28] Bai H L, Jiang E Y and Wang C D 1996 *J. Appl. Phys.* **80** 1428
[29] Vidano R P and Fischbach D B 1981 *15th Biennial Conference on Carbon* ed F L Vogel and W C Foresman (University Park, PA: American Carbon Society) extended abstracts, p 468
[30] Chen M Y, Li D, Lin X, Dravid V P, Chung Yap-Wah, Wong Ming-Show and Sproul W D 1993 *J. Vac. Sci. Technol.* A **11** 521